Nanomechanics of slip avalanches in amorphous plasticity

Penghui Cao [a,*], Karin A. Dahmen [b], Akihiro Kushima [a,f], Wendelin J. Wright [c], Harold S. Park [d], Michael P. Short [a], Sidney Yip [a,e,*]

[a] Department of Nuclear Science and Engineering, Massachusetts Institute of Technology, Cambridge, MA 02139, United States
[b] Department of Physics, University of Illinois at Urbana Champaign, Urbana, IL 61801, United States
[c] Department of Mechanical Engineering, Department of Chemical Engineering, Bucknell University, Lewisburg, PA 17837, United States
[d] Department of Mechanical Engineering, Boston University, Boston, MA 02215, United States
[e] Department of Materials Science and Engineering, Massachusetts Institute of Technology, Cambridge, MA 02139, United States
[f] Advanced Materials Processing and Analysis Center, Department of Materials Science and Engineering, University of Central Florida, Orlando, FL 32816, United States

ARTICLE INFO

ABSTRACT

Discrete stress relaxations (slip avalanches) in a model metallic glass under uniaxial compression are studied using a metadynamics algorithm for molecular simulation at experimental strain rates. The onset of yielding is observed at the first major stress drop, accompanied, upon analysis, by the formation of a single localized shear band region spanning the entire system. During the elastic response prior to yielding, low concentrations of shear transformation deformation events appear intermittently and spatially uncorrelated. During serrated flow following yielding, small stress drops occur interspersed between large drops. The simulation results point to a threshold value of stress dissipation as a characteristic feature separating major and minor avalanches consistent with mean-field modeling analysis and mechanical testing experiments. We further interpret this behavior to be a consequence of a nonlinear interplay of two prevailing mechanisms of amorphous plasticity, thermally activated atomic diffusion and stress-induced shear transformations, originally proposed by Spaepen and Argon, respectively. Probing the atomistic processes at widely separate strain rates gives insight to different modes of shear band formation: percolation of shear transformations versus crack-like propagation. Additionally a focus on crossover avalanche size has implications for nanomechanical modeling of spatially and temporally heterogeneous dynamics.

© 2018 Elsevier Ltd. All rights reserved.

1. Introduction

Although the plastic response of amorphous solids such as metallic glasses has been under study for some time (Cheng and Ma, 2011a; Hufnagel et al., 2016; Schuh et al., 2007a), quantitative details of the elementary deformation processes at the nanoscale are still lacking. Recent compression (Antonaglia et al., 2014a,b; Harris et al., 2016; Mukai et al., 2002; Sun et al., 2012; Wright et al., 2001) and nanoindentation (Cheng et al., 2014; Golovin et al., 2001; Jiang and Atzmon, 2003; Schuh and Nieh, 2003; Schuh et al., 2002) experiments have focused on the dynamical evolution of slip avalanches, the serrations in stress-strain behavior of a driven system. A common characteristic of serrated flow is the strain-rate sensitivity

becoming more pronounced as rates are lowered (Antonaglia et al., 2014b; Harris et al., 2016; Schuh et al., 2002, 2007a). To understand the molecular mechanisms of stress relaxation, quantitative details available from molecular simulations would be useful. However, the simulations performed to date (Albe et al., 2013; Cheng and Ma, 2011b; Sha et al., 2017; Shi and Falk, 2005; Shimizu et al., 2007; Zhou et al., 2015) are constrained to strain rates higher by several orders of magnitude than those studied experimentally or treated by mechanics-based modeling.

In this work, we implement an atomistic simulation algorithm that can reach timescales in the range of experiments. We study a metallic glass model in uniaxial compression at a relatively low temperature of $0.33T_g$, where T_g is the glass transition temperature, with a focus on the effects of strain rate. Our results reveal a scenario of dynamical evolution in which system deformation occurs through a series of small and large discrete stress relaxations. Even though this behavior is well known at the constitutive level, details of the individual and collective molecular processes have not been probed at low strain rate previously. By analyzing the spatial distributions of the local deviatoric strain and the non-affine atomic displacement during the evolution, we find the small avalanches to be spatially isolated processes occurring intermittently, and the large avalanches to be highly collective processes associated with the formation and subsequent evolution of a spontaneously formed shear band. The significance of avalanche size emerges naturally from visualizing the spatial and temporal correlations in local strain and atomic diffusion, as well as from the statistics on the magnitude of the stress relaxation, number of atoms involved, atom mobility and avalanche duration. Prior to the onset of yielding, only strain-rate sensitive small avalanches are observed. A large avalanche first appears at the onset of yielding. During subsequent flow, large avalanches occur intermixed with small avalanches. The regularly appearing large avalanches are associated with shear localization, just as observed in experiments (Antonaglia et al., 2014a; Wright et al., 2016) and described by an analytic mean field modeling approach (Dahmen et al., 2009). The atomistic processes during yielding and subsequent plastic flow reveal shear band formation can occur as percolation of shear transformation events at high strain rates and crack-like propagation at low strain rates. Our findings also provide nanoscale details to complement current experimental and theoretical studies, enabling a more quantitative characterization of the elementary processes of amorphous plasticity.

We begin in Section 2 with a description of the model metallic glass and a metadynamics method for atomistic simulation at a prescribed strain rate. The algorithm we implement is based on a method called ABC (autonomous basin climbing) first applied to compute the shear viscosity of supercooled liquids (Kushima et al., 2009). The saddle points along the obtained trajectory are the essential results that allow the simulation to proceed according to transition-state theory rather than Newtonian dynamics. The stress-strain curves simulated at three significantly different strain rates are presented in Section 3, each showing an elastic response up to yielding, followed by plastic flow with a series of major and minor stress drops. We give particular attention to the strain rate typical of experimental measurements. In the vicinity of yielding one sees clearly the spontaneous formation of a band-shaped region of localized shear from the local atomic strain maps. Once formed, this structural defect completely dominates the evolution of the subsequent serrated flow. In Section 4 we examine the statistical significance of the magnitude of stress relaxation, i.e. the avalanche size, as an indication of the different modes of deformation response, and also an indication of strain-rate effects. We find a natural separation between small and large avalanches that becomes a continuing theme throughout our study. The atomic-level deformations and atomic displacements are also presented which show a considerably more dominant role for the large avalanches. In Section 5 we give an interpretation of nonlinear response to the existence of a stress relaxation seen from the simulation data in various forms. In Section 6 we investigate the nanoscale processes of shear-band formation by combining mean field modeling analysis and mechanical testing experiments with the present simulation at strain rates typical of experiments or molecular dynamics simulations. In these two ranges of strain rate we find a shear band can form in a manner that can be described as crack-tip extension like and progressive percolation, respectively. Finally in Section 7 we indicate how different modeling frameworks can be unified by focusing on the nonlinear coupling between thermal and stress activations.

2. Models and methods

2.1. Simulation model

We model a metallic glass thin film using a two-dimensional binary Lennard–Jones (BLJ) mixture previously developed to study mechanical properties of amorphous solids (Falk and Langer, 1998). In this model there are two species referred to as 'a' and 'b'. The length and energy are measured in units of the potential parameters, σ_{ab} and ϵ_{ab}, respectively, while time is measured in units of $t_0 = \sigma_{ab}\sqrt{m/\epsilon_{ab}}$, with m being the mass of both 'a' and 'b' particle species. The temperature is measured in $T_0 = \epsilon_{ab}/k_b$. The glass transition temperature T_g of the model is determined to be $0.3T_0$. For conversion to absolute values we take the time units $t_0 \approx 1$ps and length units $\sigma_{ab} \approx 1$ Å (Shi and Falk, 2005).

To prepare the initial glassy configurations, we equilibrate a liquid containing varying numbers of particles (600, 2000, 10,000 and 25,000) at a high temperature of $T = 1.0T_0$ for $100,000t_0$ under a NVT (constant number of particles, volume, and temperature) ensemble. Periodic boundary conditions are applied in x and y directions. Subsequent to equilibration, the system temperature is quenched to a low temperature of $T = 0.1T_0$ (i.e. $0.33T_g$) at a cooling rate that is as slow as possible using MD simulation (1.8×10^{-6} in LJ units). To model a uniaxial compression experiment, two free surfaces in the x-direction are created by removing the periodic boundary condition to give two stress-free surfaces during compression. We further relax the amorphous systems for another $100,000t_0$ to a state of zero average stress using an NPT (constant

number of particles, pressure, and temperature) ensemble. For each system size, four glassy structures are prepared using this procedure. Our discussion will mainly focus on the system size of 10,000, unless explicitly indicated otherwise.

2.2. Metadynamics simulation at constant strain rate

The traditional molecular dynamics method is limited to a high strain rate regime, above $10^6 s^{-1}$ (Zhu et al., 2008). On the other hand, experimental studies on compression testing of metallic glass have been performed at strain rates typically slower than $10^{-1} s^{-1}$ (Schuh et al., 2007b). In this work we implement a metadynamics algorithm that enables us to bridge the gap in strain rates from traditional MD to those seen experimentally (Cao et al., 2012; Fan et al., 2013a; Kushima et al., 2011, 2009). We begin with an atomic configuration of the metallic glass at $0.33 T_g$ prepared by the procedure described above. We select a strain-rate value for the simulation, and use the transition-state theory expression $\dot{\epsilon} = \dot{\gamma}_0 \exp(-E_b / k_B T)$ to determine a value for the activation barrier E_b, where γ_0 is the attempt frequency prefactor and k_B is the Boltzmann constant. The value of $\gamma_0 = 0.5 t_0^{-1}$ ($\sim 10^{12} s^{-1}$) taken in this work has been previously determined to reproduce high strain rate MD simulation results (Cao et al., 2014a, 2013). After determination of the activation barrier E_b for a strain rate $\dot{\epsilon}$, we perform the following steps:

1. Perform energy minimization to bring the system to the nearest local energy minimum state.
2. Run the autonomous basin climbing (ABC) algorithm (Cao et al., 2012; Kushima et al., 2009) to generate a transition-state pathway (TSP) trajectory consisting of local energy minima and saddle points, stopping the ABC simulation when an activation energy barrier greater than E_b is found.
3. Examine the local energy minima explored by the ABC algorithm, and perform a standard Monte Carlo (MC) run to pick the most likely state according to the probability $p = \exp(\Delta E_{(i,j)} / k_B T)$, where $\Delta E_{(i,j)}$ is the energy difference between local minima i and j. Save the associated atomic configurations.
4. Apply a small strain increment $\Delta \epsilon = 10^{-4}$ to the system, perform energy minimization and repeat steps 1–3. Each step thus contributes a strain increment $\Delta \epsilon$ to the overall imposed strain ϵ. The associated atomic configurations stored in the process can be used to calculate the corresponding single-atom displacement and the local deviatoric strain. The iteration continues until the strain ϵ reaches 18%.
5. For quasistatic (QS) simulation, $E_b = 0$, so there is no need to run steps 2 and 3. The simulation thus consists of iterating on steps 1 and 4, performing energy minimization after each strain increment.

The ABC algorithm we used here was designed to circumvent the timescale limitation of traditional MD. It has been used previously in studies of material creep (Cao et al., 2017; Lau et al., 2010), slow strain rate deformation of imperfect crystals (Fan et al., 2013a), amorphous solids (Cao et al., 2014a,b) and nanostructures (Tao et al., 2018; Yan and Sharma, 2016). Recently the metadynamics approach based on the ABC algorithm has been implemented to study plastic deformation in amorphous Li-Si nanostructures (Yan et al., 2017).

2.3. Calculation of atomic-level strain and non-affine displacement

We consider the deviatoric strain $D_{\min}^2$ as an indicator for plastic deformation. The local strain $D_{\min}^2$ associated with an atom during a system-level strain increment $\delta \epsilon$ is computed as Falk and Langer (1998) and Shimizu et al. (2007)

$$D_{\min}^2(\epsilon, \epsilon + \delta \epsilon) = \sum_{i=1}^{n} [\mathbf{X}_i(\epsilon + \delta \epsilon) - \mathbf{X}_0(\epsilon + \delta \epsilon) - \mathbf{J} \times (\mathbf{X}_i(\epsilon) - \mathbf{X}_0(\epsilon))]^2 \tag{1}$$

where the subscript 0 denotes the designated atom and index i iterates over all atoms within the interaction cutoff relative to the reference atom. $\mathbf{X}_i(\epsilon)$ is the position of the ith atom at compressive strain ϵ, and $\mathbf{J}$ is the affine deformation tensor that transforms a nearest neighbor separation, $\mathbf{X}_i(\epsilon) - \mathbf{X}_0(\epsilon)$, to an expected separation during strain interval $[\epsilon, \epsilon + \delta \epsilon]$. The best-fit deformation tensor $\mathbf{J}$ is extracted by minimizing $D_{\min}^2(\epsilon, \epsilon + \delta \epsilon)$. The minimum value of $D_{\min}^2(\epsilon, \epsilon + \delta \epsilon)$ is the local deviatoric strain, which identifies local plastic shear transformations.

To probe the local dynamics of individual atoms associated with system-level stress relaxation, we compute the non-affine displacement for each atom. For a strain interval $[\epsilon, \epsilon + \delta \epsilon]$, the non-affine displacement of an atom is computed by subtracting the affine displacement

$$\delta u_\alpha(\epsilon, \ \epsilon + \delta \epsilon) = X_\alpha(\epsilon + \delta \epsilon) - F_{\alpha\beta} X_\beta(\epsilon) \tag{2}$$

where the Greek indices α and β indicate the Cartesian components and $F_{\alpha\beta}$ is the deformation gradient. It is related to a system-level deformation strain increment by $F_{\alpha\beta} = 1 + \delta \epsilon_{\alpha\beta}$.

3. Yielding onset and serrated flow

The responses of system-level stress to uniaxial compression at three separate strain rates are shown in Fig 1(a). The curve QS (quasistatic) (Falk and Maloney, 2010) is obtained by potential energy minimization, which is effectively the limit of high strain rate (Cao et al., 2014a; Fan et al., 2013a). The other two curves correspond, respectively, to constant strain
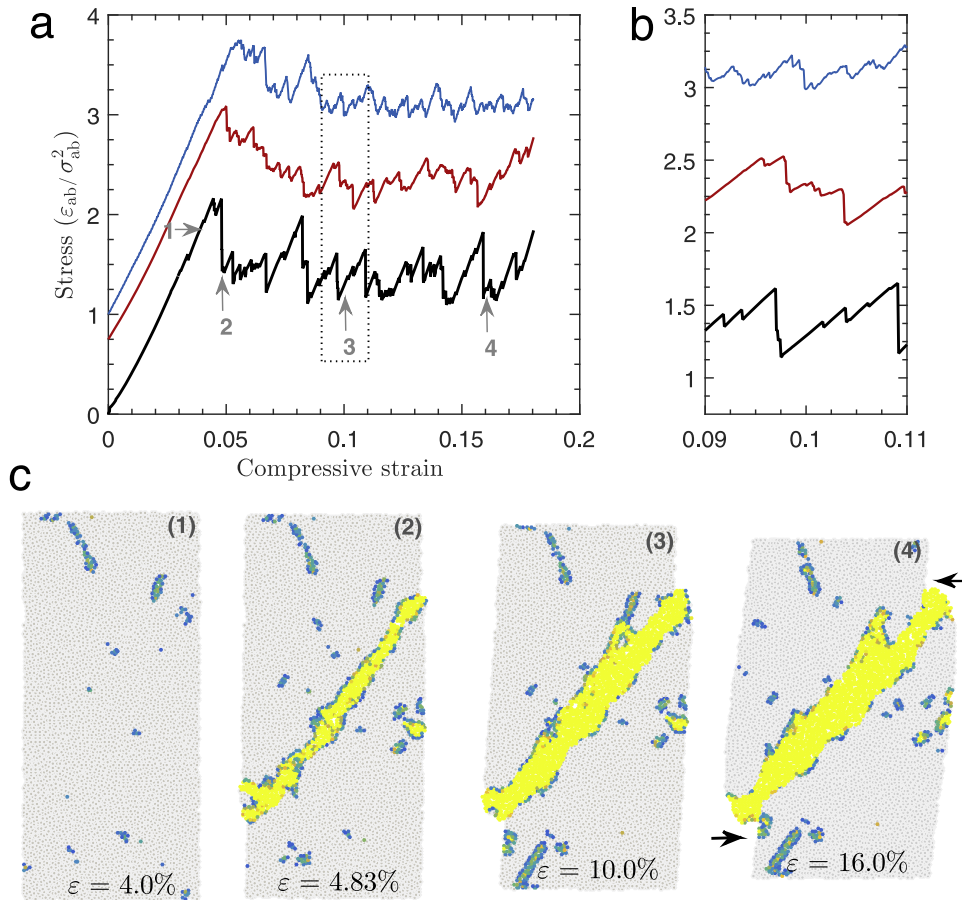
Fig. 1. (a) Stress-strain response obtained at three strain rates: QS (top), $2.2 \times 10^7 s^{-1}$ (middle), and 4.6×10^{-2} s^{-1} (bottom). The two upper curves have been shifted vertically by 1.0 and 0.75, respectively, to facilitate visual inspection. Arrows indicate the four stages of deformation corresponding to the four panels shown in (c). (b) Enlarged view of dotted box in (a). (c) Deviatoric strain distributions in the elastic response regime, after yielding and during the flow stage at a strain rate of $4.6 \times 10^{-2} s^{-1}$. The red spheres indicate atoms subjected to large deviatoric strain, and atoms with strain $D_{\min}^2 < 1$ are colored gray. The arrows point to surface steps at strain of 16.0%. (For interpretation of the references to color in this figure legend, the reader is referred to the web version of this article.)

rates of $2.2 \times 10^7 s^{-1}$ and 4.6×10^{-2} s^{-1}, which are typical of conventional MD simulations and laboratory mechanical testing, respectively.

The overall response at each strain rate shows initially elastic loading up to a yield point, followed by a series of stress drops of varying magnitudes. The effects of strain rate are first a lowering of the entire stress-strain curve as the strain rate decreases from QS to MD to laboratory testing. Secondly, a significant sharpening of the serrations occurs in this progression of strain rates. The variation of the peak (yield) stress with strain rate, known as the stress overshoot, is also evident. These qualitative features follow from noting that a slower strain rate allows the system more time to respond dynamically; this dynamic response involves local fluctuations and redistributions at the nanoscale that would be reached by further analysis.

In Fig. 1(b) portions of the flow curve at the three strain rates are shown in greater detail to illustrate the significant sharpening in avalanche response as the strain rate is lowered (Antonaglia et al., 2014b; Maaß et al., 2011). At the lowest strain rate, we see well-resolved intermittent minor relaxations interspersed between large events throughout the entire flow regime. Similar behavior, suggesting a distinction between small and large avalanches, is observed experimentally (Antonaglia et al., 2014a; Maaß et al., 2011; Wright et al., 2016).

In Fig. 1(c) we show the corresponding deformations at the lowest strain rate associated with the onset of yielding and subsequent flow. In the four panels one sees the spatial distributions of atomic sites with high deviatoric strain, color coded to indicate the magnitude of $D_{\min}^2$. The distributions are cumulative strains (with reference to the initial undeformed configuration) during compression at the four numbered stages labeled in Fig. 1(a): during elastic loading (point 1), after yielding (2), and during serrated flow (3–4). At 4% strain, we see only a few high-strain sites distributed rather randomly. Immediately after the onset of yielding, at 4.83% strain, a band of high-strain sites spanning the system has clearly formed (see Section 6 for the discussion of shear band formation). Notice also the appearance of a surface step. After the appearance of the shear band, the subsequent plastic flow is essentially dominated by this shear localized region, involving sliding and
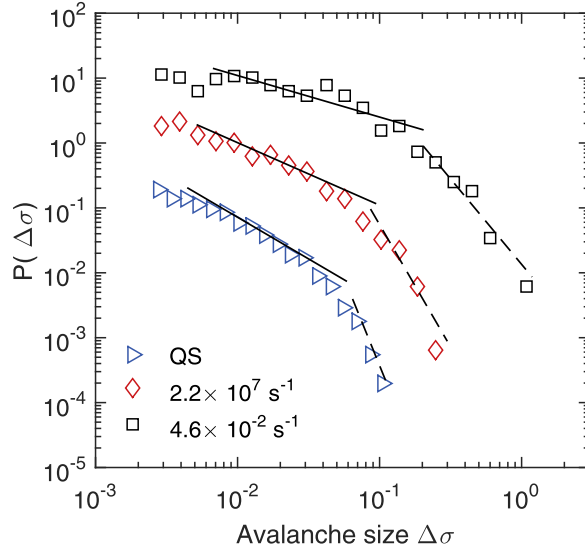
Fig. 2. Probability distribution of stress drops $p(\Delta\sigma)$ at various strain rates. The top two curves have been shifted vertically to facilitate visual inspection by $\times 10$ and $\times 100$, respectively.

thickening. For example, with further compression through 10%–16% strain, the shear band has expanded in thickness as shown in the third and fourth panels of Fig. 1(c). Correspondingly, the edge steps have become larger to accommodate the increased strain in the system (Shan et al., 2008). These quantitative nanoscale results, derived from the simulation at low strain rate, have not been available heretofore.

The scenario of a spatial distribution of localized strain production shown in Fig. 1(c) demonstrates that the process of yielding at the nanoscale is associated with the formation of a single localized (but system spanning) region of high strain. Once this extended region of deformation is established, it dominates the subsequent stress relaxation response by giving rise to a series of small and large avalanches. In particular, the first three panels in Fig. 1(c) clearly reveal the connection between the first large avalanche with the onset of system yielding.

4. Spatial and temporal characteristics of avalanches

4.1. Major and minor avalanches

Since stress relaxations (avalanches) are a natural part of the system-level behavior, their dependence on strain rate immediately becomes a subject of interest. Fig. 2 shows the statistical distribution results that suggest the avalanche size, i.e. the magnitude of the stress drop, plays a central role in characterizing the underlying molecular processes associated with the avalanches. The probability distributions of avalanche sizes $P(\Delta\sigma)$ during steady-state flow at three strain rates are shown. It can be seen the larger avalanches are more probable as the strain rate decreases. This sensitivity is consistent with our interpretation of Fig. 1(b). By looking at the $p(\Delta\sigma)$curves, one can observe a crossover that starts from a shallow slope for small avalanches to a steeper slope for large avalanches. A crossover in the power-law exponent was reported in a recent creep flow experiment, in which the onset of plastic deformation is linked to a transition from random activity to shear band sliding (Krisponeit et al., 2014).

In the scatter plot of Fig. 3 we see similarly the large avalanches have longer durations, the behavior being more pronounced at low strain rate. When the strain rate varies from $10^7 s^{-1}$ to $10^{-2} s^{-1}$, we observe a separation of larger avalanches from small ones at a threshold value of $\Delta\sigma_c \sim 0.1$. We will demonstrate below that the large avalanches play a key role in controlling the dynamics of the stress relaxations.

4.2. Nanoscale maps of local atomic strain and nonaffine atomic displacements

To probe the nanoscale deformation and flow processes associated with an avalanche, we examine two dynamical order parameters that can be extracted from the atomic configurations, the deviatoric strain $D^2_{\min}$ and the non-affine atomic displacement. Their spatial distributions can be visualized at each stress drop during the plastic flow. Moreover, the results can be resolved according to avalanche size $\Delta\sigma$, so the small and large avalanches can be examined separately.

Fig. 4 shows the spatial maps of $D^2_{\min}$ for small and large avalanches at the steady-state flow stage of deformation. In contrast to Fig. 1(c) these strain distributions are not cumulative, rather they are incremental atomic strains corresponding
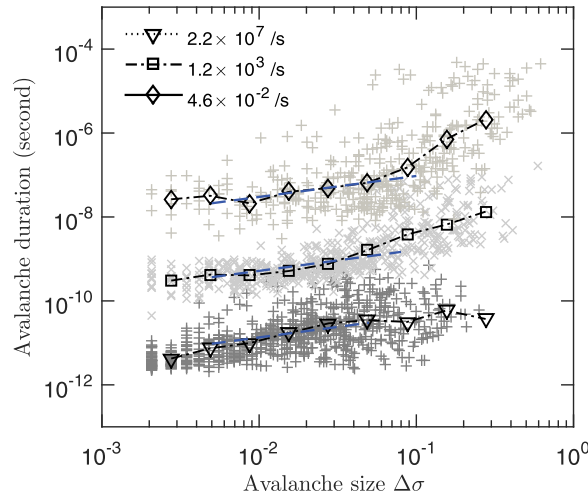
Fig. 3. Correlation of avalanche duration with avalanche size at various strain rates. The dashed lines are the mean field model predictions.
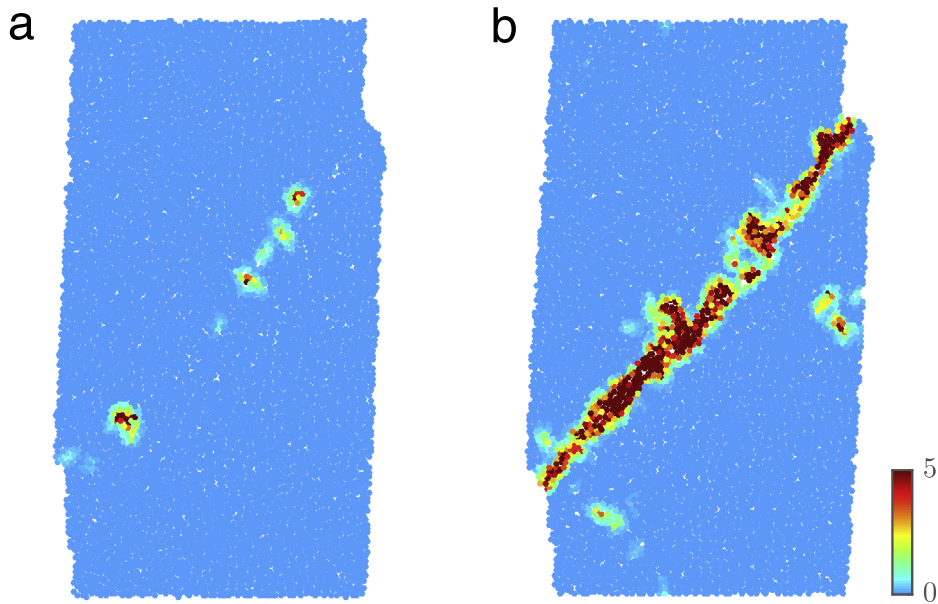

Fig. 4. Visualization of local plastic strains associated with two typical avalanches, small (a) and large (b). Atoms are color coded by the magnitude of $D_{\min}^2$. The imposed strains in the two cases are 8.3% and 9.7%, respectively.

to a particular stress drop event. On the time scale of the entire compression experiment, the events can be regarded as effectively instantaneous at the particular deformation stage indicated by the current strain.

In Fig. 4(a), which pertains to small avalanches, one sees a few local sites of significant strain magnitude. This indicates that during a minor stress drop, there is relatively little activity involving localized shear transformations and the few activated sites are spread out along the established shear band. In contrast, as seen in Fig. 4(b), major stress relaxations involve a large number of activated sites at high strain magnitudes, clustered along a characteristic band-like region. Comparing Fig. 4(a) and (b), one has a clear picture of the different roles that small and large avalanches play in maintaining serrated flow. Recall from Fig. 3 that high strain rates do not allow the large avalanches to develop fully. Thus the importance of performing simulations at low strain rates is evident.

The atomic configurations associated with the deformation response also provide information about the dynamics of a single atom. Through the non-affine displacements, we can assess atomic motions associated with internal relaxation during system flow. In Fig. 5 we again see the distinction between small and large avalanches now visualized through the non-affine atom displacement. Comparing these results with the distributions of plastic strain production, we have a consistent picture of the molecular processes associated with serrated flow, resolved between small and large avalanches, and between the single-particle (diffusion) and collective (cluster deformation) degrees of freedom. The processes are clearly spatially
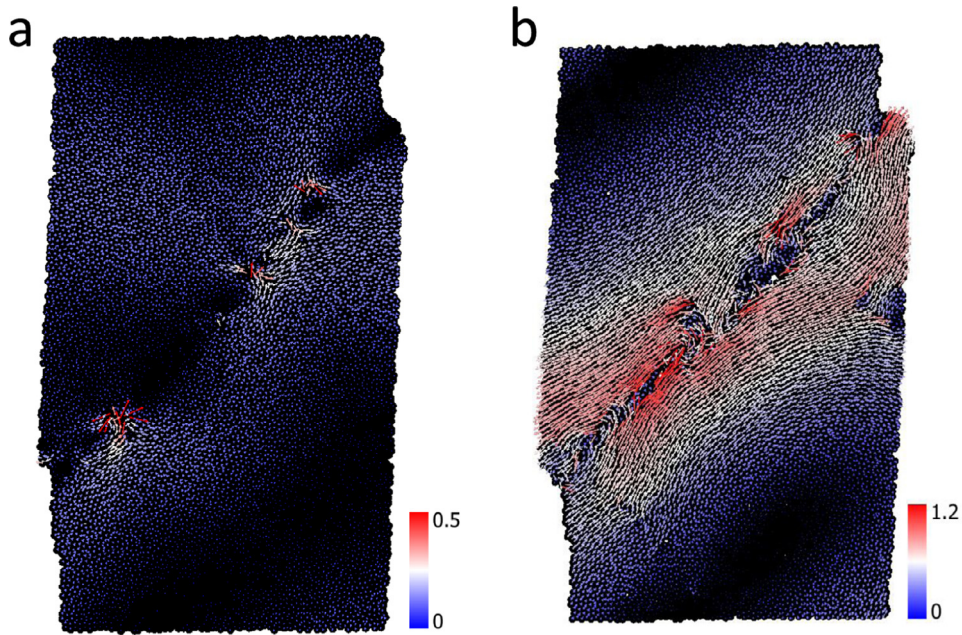
Fig. 5. Visualization of non-affine displacement associated with small (a) and large (b) avalanches. Arrows are color coded by the non-affine displacement magnitude. Note that the color scale is different for (a) and (b). The imposed strains in the two cases are 8.3% and 9.7%, respectively.
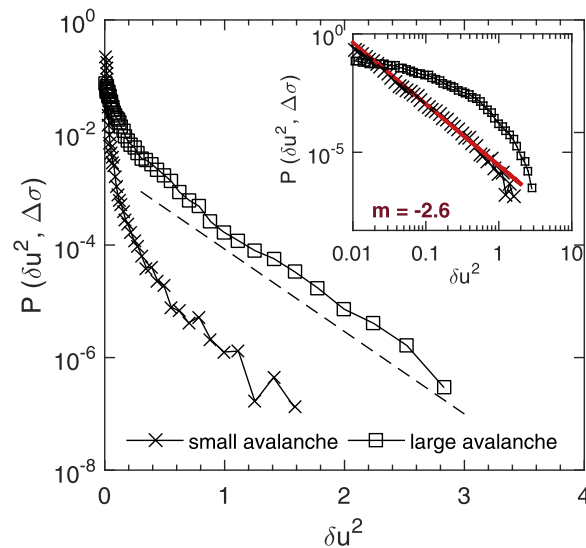

Fig. 6. Probability distributions $P(\delta u^2, \Delta\sigma)$ of individual particle displacement δu^2 for small avalanches ($\Delta\sigma \in (0.02, 0.08)$) and large avalanches ($\Delta\sigma \in (0.2, 0.7)$). The distribution $P(\delta u^2)$ of large avalanches is terminated with a exponential tail. The inset shows a log-log plot where the small avalanches demonstrate a power-law decay with an exponent of -2.6.

heterogeneous on the nanometer scale and temporally intermittent on the scale of milliseconds. Such new details provide meaningful complements to current studies of the mechanisms of amorphous plasticity, based on combining theoretical modeling (Antonaglia et al., 2014a) with high temporal resolution mechanical testing (Wright et al., 2016).

The behavior of deviatoric strain and non-affine displacement reaffirm the fundamental distinction between different models of relaxation (see discussion). Additional analysis can be made of the statistical distributions of the order parameters. Fig. 6 shows the probability distribution of the non-affine mean square displacement $P(\delta u^2)$ for the two types of processes. The distribution for the minor avalanches shows a more rapid decay that can be described as a power law with exponent -2.6. In contrast, the major relaxations are more persistent, with a tail that is essentially exponential. Power-law and exponential distributions indicate further distinctions between relaxation processes involving single atom displacements. Similar results have been discussed in confocal microscopy experiments of non-affine fluctuations in sheared colloidal glasses where
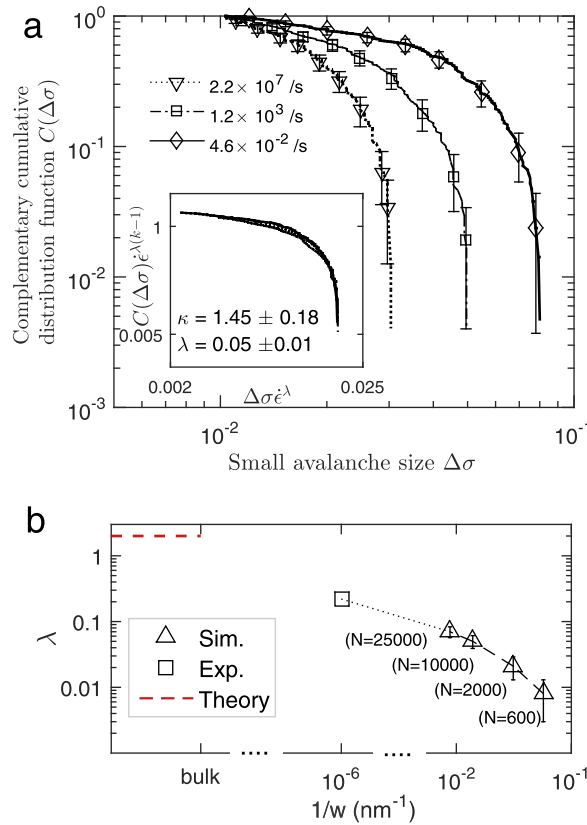
Fig. 7. (a) Complementary cumulative distribution functions (CCDF) of small avalanche size for system size of 10,000 at various strain rates: $2.2 \times 10^7 s^{-1}$ (dotted line), $1.2 \times 10^3 s^{-1}$ (dashed line) and $4.6 \times 10^{-2} s^{-1}$ (solid line). The CCDF gives the probability of finding a stress drop size larger than $\Delta\sigma$. The inset shows CCDFs and stress-drop sizes rescaled by the appropriate $\dot{\epsilon}$ dependent scaling expression, which yields the exponent values of $\kappa = 1.45 \pm 0.18$ and $\lambda = 0.05 \pm 0.01$. (b) Exponent λ as a function of system width $1/w$. N is the number of atoms in the simulation system. Mean-field theory is the limiting behavior of a large system. The experimental data are obtained from microscale metallic glass compression testing (Antonaglia et al., 2014b).

power-law distributions with an exponent of -2.8 are observed (Chikkadi and Schall, 2012). This conforms with our minor relaxation results in Fig. 4(a). Molecular dynamics simulations have probed the evolution of local deformation in terms of displacement and strain distributions. In the former an exponential tail is interpreted to signify the contributions from a more strongly sheared region (Maloney and Robbins, 2008), which is what we observe here.

4.3. Scaling behavior of small avalanches

The statistical behavior of the avalanche size can be analyzed using theoretical predictions with appropriate attention to the different conditions between nanoscale simulation and continuum models. According to a simple mean field model each avalanche is the manifestation of slipping weak spots, i.e. a slipping weak spot can trigger other weak spots to slip and so on; if the weak spots weaken during their slips, then the scaling of the slips that traverse through the system should change (Dahmen et al., 2009; 2011). Small and large slips are predicted to have different scaling behavior. For the small avalanche size distribution, a scaling form of $C(\Delta\sigma)$ with strain rate $\dot{\epsilon}$, $C(\Delta\sigma, \dot{\epsilon}) = \dot{\epsilon}^{\lambda(\kappa-1)} C'(\Delta\sigma\dot{\epsilon}^\lambda)$ is derived (Dahmen et al., 2009; 2011), where κ is a universal power exponent, λ measures the strain-rate sensitivity of small avalanches and $C'(\Delta\sigma\dot{\epsilon}^\lambda)$ is a universal scaling function that can be tested by performing a scaling collapse (Antonaglia et al., 2014b). The collapse of our data on small avalanche distributions is shown in the inset of Fig. 7(a). The obtained value of $\kappa = 1.45$ is close to the mean field prediction of 1.5. Other models and molecular dynamics simulations in $d = 2$ dimensions have yielded values for κ slightly below 1.5 in the over-damped limit at zero temperature, in the adiabatic limit (Lin et al., 2014; Salerno et al., 2012). The value of λ for nanoscale simulation is seen to be significantly smaller than the mean-field value. Physically λ is a size-dependent measure of the strain-rate sensitivity of the small avalanche distribution, having a value of 2 in the mean field theory, which is the limit of large systems. To probe the system-size effect on λ, we have studied different system sizes ranging from 600 atoms to 25,000 atoms. We found the exponent λ increases with increasing system size as shown in Fig. 7(b). From mechanical test data at the millimeter scale, λ has been found to be 0.22 (Antonaglia et al., 2014b). Thus, we see a systematic variation in λ, from the nanoscale to the micrometer scale, and the continuum limit.
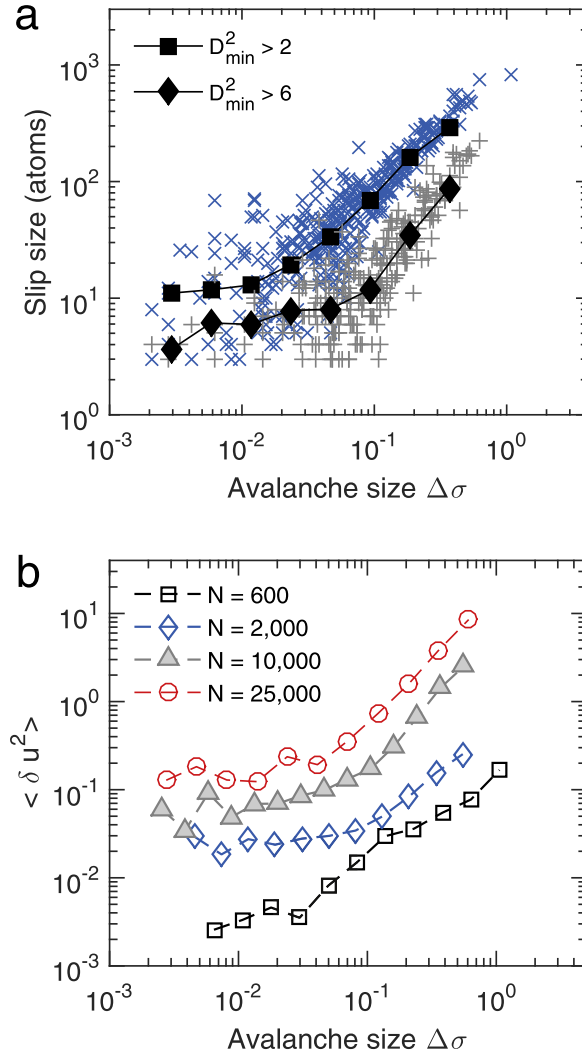
Fig. 8. (a) Correlation of the slip area (number of atoms) with avalanche size at a strain rate of 4.6×10^{-2} s^{-1} for system size of 10,000. The filled symbols are average values with solid lines drawn to guide the eye. Black 'square' and black 'diamond' symbols denote the number of atoms involved in an avalanche whose local deviatoric strain D^2_{min} is larger than 2 and 6, respectively. The value of D^2_{min} serves as a threshold strain for defining the number of atoms involved in an avalanche. (b) Non-affine mean square displacement $\langle \delta u^2 \rangle$ as a function of stress drop size $\Delta \sigma$ for a variety of system sizes. The top three curves (N = 2000, 10,000 and 25,000) have been shifted vertically to facilitate visual inspection.

5. Interpretation of nonlinear accelerated response

Throughout this work we have encountered various simulation results that suggest a natural distinction exists between small and large avalanches as measured by the magnitude of the stress relaxation. Recall in Fig. 4 we noted a threshold avalanche size, $\Delta \sigma_c \sim 0.1$, which effectively distinguishes two regimes of stress relaxation response. In Fig. 8 we demonstrate further that the notion of a threshold $\Delta \sigma_c$ is quite robust when other measures of deformation response are also taken into account. Fig. 8(a) is a scatter plot of the correlation between the number of atoms estimated to be involved in a given avalanche with avalanche size $\Delta \sigma$. The number of atoms in highly strained regions increases rapidly when the avalanche size exceeds 0.1. A pronounced correlation between large avalanches and the extent of plastic slip is seen to be consistent with the association of large avalanches with the most intense sites of strain production. In Fig. 8(b) we plot the variation of non-affine mean square displacement with avalanche size for the four simulation system sizes. The results for the two large systems appear to converge at the lower end of the small avalanches, and also at the higher end of the large avalanches, indicating a natural separation between small and large avalanches when system size is larger than 2000. For the smallest system size of 600, more scatter in the data and ambiguity in the crossover between small and large avalanches can be expected due to the statistical nature of the atomistic processes. In comparing with slip size (number of atoms involved in large plastic deformation), we see the threshold notion extends equally well to atom mobility as a form of response.

The distinction of avalanche size has been recently discussed through a combination of mean-field modeling and high-resolution mechanical testing (Antonaglia et al., 2014a; Wright et al., 2016). Small and large avalanches have been interpreted to indicate processes of progressive deformation and simultaneous shear, respectively. Both processes are assumed to involve stress relaxations associated with a shear band. Because mechanical testing is much more spatially coarse-grained than the nanoscale simulation, we need to keep this in mind in discussing deformation and flow processes in the vicinity of a single strain localized band-like region at a constant strain rate.

The fact that the system response is different for avalanches below and above the threshold implies the existence of two response regimes. The actual evolution of avalanche size as shown in Fig. 1(a), suggests the small avalanches can be regarded as precursor events or an incubation stage leading up to the occasional major relaxation event. We see the large avalanches as a form of nonlinear response involving the concerted action of thermally activated atomic diffusion and stress-activated shear of local clusters of atoms. Such responses are characterized by spatial and temporal fluctuations that have been referred to as dynamical heterogeneities. Recognition of this kind of response can stimulate further theoretical work in modeling the weakening mechanism that underlies the onset of avalanches. Again we note that proper simulation of the large avalanches requires strain rates in the experimental range.

6. Avalanches and shear band formation

Shear banding is a ubiquitous mode of plastic deformation that is particularly important in metallic glasses (Greer et al., 2013). We will now consider how the combination of mean-field modeling and mechanical tests with the metadynamics simulation findings can contribute to elucidating the initial stage of shear-band formation.

6.1. Shear-band formation in metadynamics simulation

In this work we observed at low strain rate the formation of a shear band at the onset of yielding as well as its evolution during subsequent flow. By correlating the atomistic processes during the evolution of avalanche behavior, we are able to distinguish two types of shear-band formation: percolation of shear transformations at high strain rate and crack-like prop-agation at low strain rate. The first mode is observed when small avalanches dominate the mechanical response. Fig. 9(a) depicts the sequence of shear band formation through the accumulation of many shear transformation events. At the com-pressive strain ε of 6.85%, a number of shear transformations events have been activated with several appearing along the maximum shear stress direction. With concentration increasing with further strain, $\Delta\varepsilon = 0.19\%$, the sites begin to merge into an extended region. Upon another strain increase of $\Delta\varepsilon = 0.47\%$, a shear band spanning the system is formed. This scenario of shear band formation (homogeneous manner) is mainly due to the accumulation and percolation of localized plastic shear events, manifested at the system level by a series of small avalanches occurring at strain rates typical of MD simulation.

In contrast to shear banding through progressive percolation, we find another mode, which operates at experimental strain rates, namely abrupt, crack-like extension. In this case shear band formation is mediated by large avalanches as shown in Fig. 9(b). At the strain ε of 4.80%, the localized regions of shear appear in the form of discrete shear-weakened sites. At the first large avalanche relaxation, which occurs at $\Delta\varepsilon = 0.01\%$, an extended region of shear localization is formed. With the occurrence of the closely following second large avalanche ($\Delta\varepsilon = 0.03\%$), the shear band region spans the entire system. After the formation of this shear band, subsequent plastic flow is primarily dominated by the evolution of this region through thickening and sliding. Thus the shear band formation mode at low strain rate is achieved through large avalanche activity, a process that is more like crack-tip extension than representative of progressive accumulation.

6.2. Shear-band formation in mean field model and experiments

By considering a simple mean field model (Dahmen et al., 2011) and mechanical testing experiments (Antonaglia et al., 2014a) in interpreting the present metadynamics simulations, we have found the results all suggest that at low strain rates, $\Delta\sigma_c$ reflects a nucleation size for the large avalanches. This means that avalanches larger than $\Delta\sigma_c$ will become unstoppable runaway events. These events propagate in a simultaneous fashion, having crack-like scaling behavior, and they only stop when they span the entire sample. On the other hand, avalanches smaller than $\Delta\sigma_c$ have different scaling behavior: they spread progressively (or pulse-like) and remain microscopic. The experimental evidence for this scenario from the mean field model (Dahmen et al., 2009) is given in Antonaglia et al. (2014a); Wright et al. (2016) and in the present paper we show that it is also very clearly visible in Fig. 1 for the metadynamics simulations. The simulations make it possible to see how the avalanches evolve in space and time. Fig. 1 also shows that at low strain rates a series of macroscopically small events precede a suddenly nucleated large runaway event that spans the entire system.

This shear band formation mechanism for slow strain rates is very different from a percolation-like scenario. For percolation-like behavior we would expect that the large events are mostly mergers of many small events that impinge on each other. In percolation we would expect to see a higher density of smaller events before the large, system-spanning event arises. In percolation we would also expect to see events with intermediate diameters that span a wide range of sizes, before the large event occurs. Here we suggest that such a percolation mechanism may indeed be seen at higher strain rates, where the avalanches are predicted to be smaller, as has been confirmed by experiments (Antonaglia et al., 2014b);
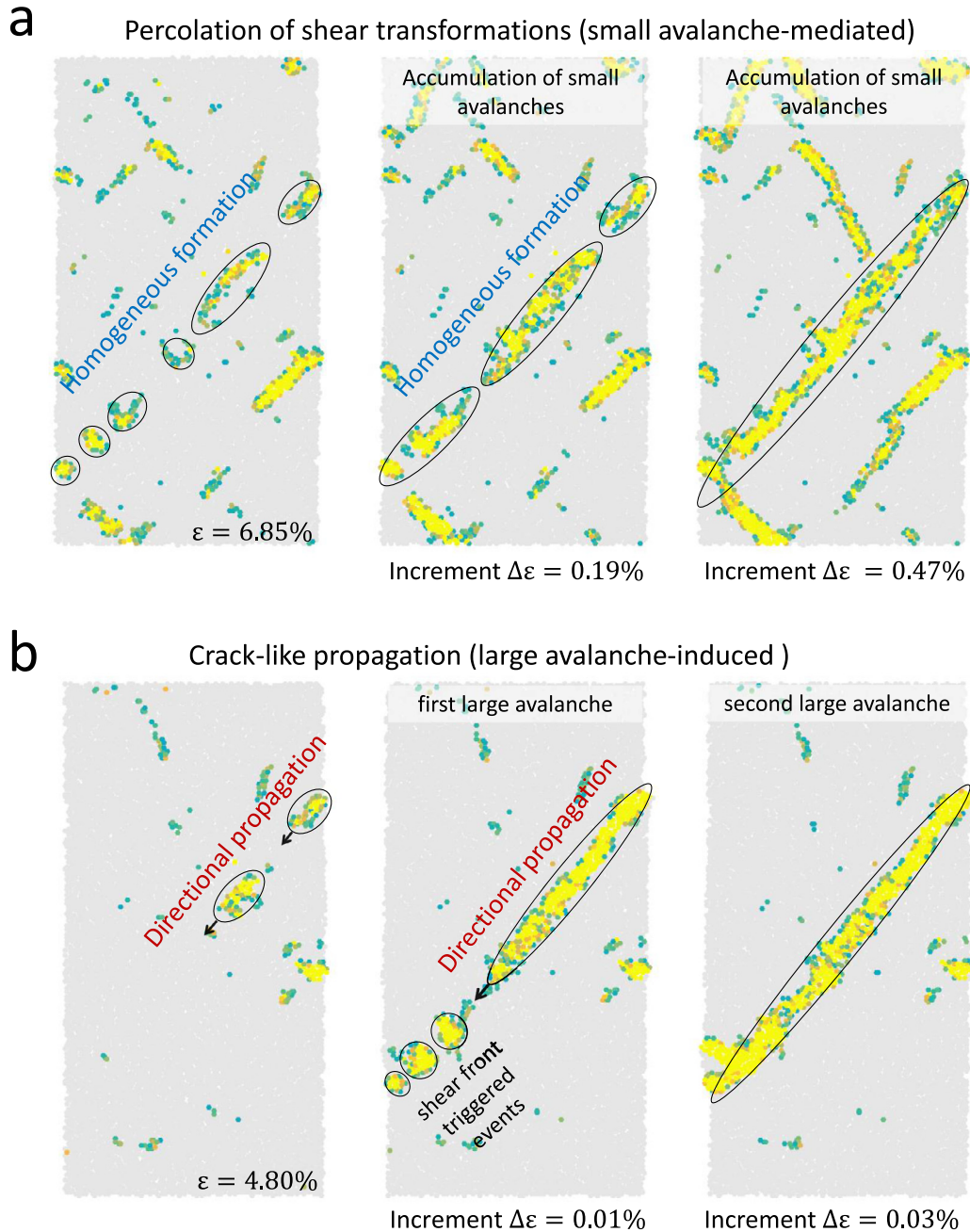
Fig. 9. Two typical shear band formation modes, shear transformation percolation observed at a high strain rate of $3.4 \times 10^9 s^{-1}$ (a) and crack-like propagation observed at a low strain rate of $4.6 \times 10^{-2} s^{-1}$ (b). The maps are colored by local deviatoric strains, and their evolutions are shown with increasing compressive strain ε. The first mode, percolation of shear transformations, is a progressive and homogeneous process, accompanied by the activation and accumulation of many local plastic events induced by a series of small avalanches. The second one is a more crack-like propagation, mediated by large avalanches.

therefore, after enough avalanches have taken place, a percolating cluster of weakened regions spanning the system exists, which then acts as an emerging shear band.

As shown in Fig. 9, the metadynamics simulations discussed here support both scenarios. For slow strain rates Fig. 1 shows mostly a few small events and no events of intermediate size that fall between the largest of the small events and the macroscopic size of the system-spanning large event. Therefore Fig. 1 is consistent with the nucleation scenario predicted by mean field theory and observed in experiments. The high-resolution experiments in Wright et al. (2016) also

show with imaging that the shear bands corresponding to large events propagate simultaneously, while the small events propagate progressively, i.e. pulse-like. Both propagation dynamics are in agreement with the predicted nucleation mechanisms of the mean field model. Simulation results indeed show that at significantly higher strain rates the slip avalanches are mostly small stress relaxation events (see Fig. 2).

6.3. Nucleation mechanisms in the mean field model

In the mean field model (Dahmen et al., 2009), the mechanism for the nucleation of avalanches at slow strain rates can be simply explained. The model assumes that each local region in the system has its own failure stress. If the local stress exceeds the failure stress, the region slips by a finite and random amount. The released stress is redistributed to the other weak spots, which can in turn be triggered to slip and so on, leading to a domino-like slip avalanche. When all weak spots are below their failure threshold, the avalanche ends. As the system is further deformed at the boundaries, the stress increases again until the next slip avalanche is triggered. For brittle materials like bulk metallic glasses, it is expected that the local failure threshold is weakened after a weak spot slips. Such weakening could be a result of local dilation for example. For very slow strain rates, the weakened thresholds may reheal between the avalanches to their original strength. If a strength weakening W is introduced, it can be shown that the model predicts a nucleation avalanche size $\Delta\sigma_{\text{nucl}} \sim 1/W^2$ for the large runaway events. It is predicted by the model that the large avalanches scale like cracks. For example, the model predicts the total stress drop size to scale linearly with the slipping area for the small avalanches, while for the large events we expect that the stress drop size scales with the area of the slipping region to the 3/2 power.

At higher strain rates the avalanches remain smaller than a cutoff $\Delta\sigma_{\text{max}}$ of the avalanche size distribution. The cutoff $\Delta\sigma_{\text{max}}$ decreases for increasing strain rate as $\Delta\sigma_{\text{max}} \sim \dot{\epsilon}^{-\lambda}$ as discussed in Section 4.3. Also at sufficiently high strain rate many weaker regions in the sample can be triggered to slip in parallel. As more and more of these precursor regions are triggered to slip, they eventually percolate to form a shear band, which is a weakened region that spans the system. Since it is easier to slip in the weakened shear band region than elsewhere, the subsequent deformation essentially occurs in the shear band. The associated stress reduction stops the slip activity outside the shear band. As a result, contrary to the situation at low strain rates, at high strain rates none of the precursor slip regions ever grow large enough to reach the nucleation size $\Delta\sigma_c$ necessary to nucleate a runaway event. In other words, for sufficiently high strain rates the nucleation mechanism that is seen at slow strain rates is prevented (kinetically suppressed) and shear bands instead form via a coalescing or collapse mechanism. This weakened spanning cluster then evolves as a shear band. The model predicts that there is a crossover strain rate $\dot{\epsilon}$ at which on average the largest slipping precursor region first reaches the nucleation size for shear bands roughly at the same time that the precursors would percolate to form a weakened spanning cluster. This crossover strain rate separates the slow strain rate regime with the crack-like nucleation mechanism from the fast strain rate regime with a percolation mechanism for shear band formation. The crossover strain rate should contain information about the degree of brittleness of the material, which is given by the weakening W. For more brittle materials (larger weakening W), the model predicts that the nucleation mechanism applies to a larger range of strain rates than for less brittle materials.

The model predicts that shear band nucleation can be suppressed by any method that reduces the largest precursor size below the nucleation size. For example, the crossover from shear band nucleation to percolation can be achieved not only by increasing the strain rate, or by making the material more ductile, but also by lowering the packing fraction of particles (Dahmen et al., 2011), which could be tested for example in granular materials or for particles in a suspension.

6.4. Discussion

In addition to the formation mode of a shear band, the imposed strain rate also can be expected to affect the magnitude of the macroscopic strain increment for forming a system-spanning band. We note shear localization that propagates and spans the system from strain 7% to 7.24% (i.e. 0.24% increment) was reported in the MD study by Cao et al. (2009), while the metadynamics simulation shows system spanning localization is formed within a 0.03% strain increment (recall Fig. 9(b)). The comparison indicates the strain increase associated with system-spanning extension is appreciably reduced, by ~ 1 order of magnitude, when lowering the strain rate from the MD range to experimentally relevant strain rates. After the formation of a shear band, the following plastic-flow stage is dominated by band-related activities such as thickening and sliding. Throughout the flow stage, the minor avalanches are interspersed between larger avalanches which can be associated with the experimentally observed stick-slip shear band sliding (Cheng et al., 2009). The minor avalanches do not directly enhance the sliding of the shear band, instead they act as incubating events, while the large avalanche acts to increase the shear offset. Thus the elastic loading increment and small avalanche activities before a larger avalanche can be regarded as a 'stick' stage, and the following large avalanche behaves like a 'slip' sliding.

The foregoing discussions indicate the molecular simulations in which strain-rate effects are resolved can inform scenarios of shear-band formation and evolution in metallic glasses by further integration with theoretical modeling and experiments (Greer et al., 2013), an example being the manner in which activated transient flow defects coalesce to form persistent microstructural defects like shear bands. Other scenarios, concerning preferential nucleation at extrinsic defects and a two-stage formation process involving rejuvenation (Cao et al., 2009), are also appropriate for investigation using the approach we are discussing here.

7. Implications for theoretical modeling

By probing the molecular processes associated with the onset of slip avalanches at an experimental strain rate, we have uncovered two modes of stress relaxation, a preparatory (weakening) mode of activating several minor stress relaxations, and an abrupt release mode where a major stress drop occurs suddenly. The onset of yielding is signaled by the appearance of the first major avalanche; subsequent plastic flow then proceeds through a series of small and large relaxation events. Spatial and temporal distributions of local deviatoric strain and non-affine atom displacement, as well as the statistical distribution of avalanche size, consistently point to a characteristic size, $\Delta\sigma_c$, as a feature of serrated flow. We interpret $\Delta\sigma_c$ to be a measure separating the minor and major avalanches. Additionally, the large avalanches involve an interplay between atomic diffusion and shear deformation, thus coupling the single-particle and the collective degrees of freedom of the system.

Our recognition of the dynamical coupling between self-diffusion and collective distortion has implications for interpreting existing models of molecular mechanisms of amorphous plasticity. Spaepen has proposed atomic diffusion via local free volume to be an order parameter in describing the transition from homogeneous to inhomogeneous flow (Spaepen, 1977). Argon, on the other hand, proposed the concept of local stress-induced shear transformation as the primary mechanism of plastic deformation (Argon, 1979). The non-affine atom displacement and the local deviatoric strain distributions analyzed here can be regarded as testing the Spaepen and Argon models, respectively. In this respect, our interpretation of the large avalanches as involving both diffusion and shear deformation implies a mechanism that combines the two processes. The term shear transformation zone (STZ) has been introduced by Falk and Langer to denote a transient flow defect (Falk and Langer, 1998). STZ implicitly combines the deformation and diffusion processes of Argon and Spaepen. It remains to be studied how to relate the present results to the STZ concept. One approach could be to apply the STZ theory developed by Langer to describe the nonlinear response behavior that we have identified (Langer, 2015).

Besides the STZ theory, the availability of a method capable of simulating experimental results at physically relevant strain rates means quantitative input can be produced to guide the description of nonlinear coupling mechanisms in various theoretical frameworks, such as the extended mode-coupling theory (Gruber et al., 2016), mean-field theory with weakening model (Antonaglia et al., 2014a), and time-dependent transition-state theory approach (Fan et al., 2013b).

Acknowledgments

References

Albe, K., Ritter, Y., Şopu, D., 2013. Enhancing the plasticity of metallic glasses: shear band formation, nanocomposites and nanoglasses investigated by molecular dynamics simulations. Mech. Mater. 67, 94–103.

Antonaglia, J., Wright, W.J., Gu, X., Byer, R.R., Hufnagel, T.C., LeBlanc, M., Uhl, J.T., Dahmen, K.A., 2014a. Bulk metallic glasses deform via slip avalanches. Phys. Rev. Lett. 112 (15), 155501.

Antonaglia, J., Xie, X., Schwarz, G., Wraith, M., Qiao, J., Zhang, Y., Liaw, P.K., Uhl, J.T., Dahmen, K.A., 2014b. Tuned critical avalanche scaling in bulk metallic glasses. Sci. Rep. 4, 4382.

Argon, A.S., 1979. Plastic deformation in metallic glasses. Acta Metall. 27, 47–58.

Cao, A.J., Cheng, Y.Q., Ma, E., 2009. Structural processes that initiate shear localization in metallic glass. Acta Mater. 57, 5146–5155.

Cao, P., Li, M., Heugle, R.J., Park, H.S., Lin, X., 2012. A self-learning metabasin escape algorithm and the metabasin correlation length of supercooled liquids. Phys. Rev. E 86, 016710.

Cao, P., Lin, X., Park, H.S., 2014a. Strain-rate and temperature dependence of yield stress of amorphous solids via self-learning metabasin escape algorithm. J. Mech. Phys. Solids 68, 239–250.

Cao, P., Lin, X., Park, H.S., 2014b. Surface shear-transformation zones in amorphous solids. Phys. Rev. E 90 (1), 012311.

Cao, P., Park, H.S., Lin, X., 2013. Strain-rate and temperature-driven transition in the shear transformation zone for two-dimensional amorphous solids. Phys. Rev. E 88, 042404.

Cao, P., Short, M.P., Yip, S., 2017. Understanding the mechanisms of amorphous creep through molecular simulation. Proc. Natl. Acad. Sci. 114 (52), 13631–13636.

Cheng, L., Jiao, Z., Ma, S., Qiao, J., Wang, Z., 2014. Serrated flow behaviors of a Zr-based bulk metallic glass by nanoindentation. J. Appl. Phys. 115 (8), 084907.

Cheng, Y., Han, Z., Li, Y., Ma, E., 2009. Cold versus hot shear banding in bulk metallic glass. Phys. Rev. B 80 (13), 134115.

Cheng, Y., Ma, E., 2011a. Atomic-level structure and structure–property relationship in metallic glasses. Prog. Mater. Sci. 56 (4), 379–473.

Cheng, Y.Q., Ma, E., 2011b. Intrinsic shear strength of metallic glass. Acta Mater. 59, 1800–1807.

Chikkadi, V., Schall, P., 2012. Nonaffine measures of particle displacements in sheared colloidal glasses. Phys. Rev. E 85 (3), 031402.

Dahmen, K.A., Ben-Zion, Y., Uhl, J.T., 2009. Micromechanical model for deformation in solids with universal predictions for stress-strain curves and slip avalanches. Phys. Rev. Lett. 102 (17), 175501.

Dahmen, K.A., Ben-Zion, Y., Uhl, J.T., 2011. A simple analytic theory for the statistics of avalanches in sheared granular materials. Nat. Phys. 7 (7), 554–557.

Falk, M., Maloney, C., 2010. Simulating the mechanical response of amorphous solids using atomistic methods. Eur. Phys. J. B 75 (4), 405–413.

Falk, M.L., Langer, J.S., 1998. Dynamics of viscoplastic deformation in amorphous solids. Phys. Rev. E 57 (6), 7192–7205.

Fan, Y., Osetskiy, Y.N., Yip, S., Yildiz, B., 2013a. Mapping strain rate dependence of dislocation-defect interactions by atomistic simulations. Proc. Natl. Acad. Sci. 110 (44), 17756–17761.

Fan, Y., Yildiz, B., Yip, S., 2013b. Analogy between glass rheology and crystal plasticity: yielding at high strain rate. Soft Matter 9 (40), 9511–9514.

Golovin, Y.I., Ivolgin, V., Khonik, V., Kitagawa, K., Tyurin, A., 2001. Serrated plastic flow during nanoindentation of a bulk metallic glass. Scr. Mater. 45 (8), 947–952.

Greer, A., Cheng, Y., Ma, E., 2013. Shear bands in metallic glasses. Mater. Sci. Eng. 74 (4), 71–132.

Gruber, M., Abade, G.C., Puertas, A.M., Fuchs, M., 2016. Active microrheology in a colloidal glass. Phys. Rev. E 94 (4), 042602.

Harris, M.B., Watts, L.S., Homer, E.R., 2016. Competition between shear band nucleation and propagation across rate-dependent flow transitions in a model metallic glass. Acta Mater. 111, 273–282.

Hufnagel, T.C., Schuh, C.A., Falk, M.L., 2016. Deformation of metallic glasses: recent developments in theory, simulations, and experiments. Acta Mater. 109, 375–393.

Jiang, W., Atzmon, M., 2003. Rate dependence of serrated flow in a metallic glass. J. Mater. Res. 18 (4), 755–757.

Krisponeit, J.-O., Pitikaris, S., Avila, K.E., Küchemann, S., Krüger, A., Samwer, K., 2014. Crossover from random three-dimensional avalanches to correlated nano shear bands in metallic glasses. Nat. Commun. 5, 3616.

Kushima, A., Eapen, J., Li, J., Yip, S., Zhu, T., 2011. Time scale bridging in atomistic simulation of slow dynamics: viscous relaxation and defect activation. Eur. Phys. J. B-Condens. Matter Complex Syst. 82 (3), 271–293.

Kushima, A., Lin, X., Li, J., Eapen, J., Mauro, J.C., Qian, X., Diep, P., Yip, S., 2009. Computing the viscosity of supercooled liquids. J. Chem. Phys. 130, 224504.

Langer, J.S., 2015. Shear-transformation-zone theory of yielding in a thermal amorphous materials. Phys. Rev. E 92 (1), 012318.

Lau, T.T., Kushima, A., Yip, S., 2010. Atomistic simulation of creep in a nanocrystal. Phys. Rev. Lett. 104 (17), 175501.

Lin, J., Lerner, E., Rosso, A., Wyart, M., 2014. Scaling description of the yielding transition in soft amorphous solids at zero temperature. Proc. Natl. Acad. Sci. 111 (40), 14382–14387.

Maaß, R., Klaumünzer, D., Löffler, J., 2011. Propagation dynamics of individual shear bands during inhomogeneous flow in a Zr-based bulk metallic glass. Acta Mater. 59 (8), 3205–3213.

Maloney, C.E., Robbins, M.O., 2008. Evolution of displacements and strains in sheared amorphous solids. J. Phys. 20 (24), 244128.

Mukai, T., Nieh, T., Kawamura, Y., Inoue, A., Higashi, K., 2002. Effect of strain rate on compressive behavior of a Pd 40 Ni 40 P 20 bulk metallic glass. Intermetallics 10 (11), 1071–1077.

Salerno, K.M., Maloney, C.E., Robbins, M.O., 2012. Avalanches in strained amorphous solids: does inertia destroy critical behavior? Phys. Rev. Lett. 109 (10), 105703.

Schuh, C., Nieh, T., 2003. A nanoindentation study of serrated flow in bulk metallic glasses. Acta Mater. 51 (1), 87–99.

Schuh, C., Nieh, T., Kawamura, Y., 2002. Rate dependence of serrated flow during nanoindentation of a bulk metallic glass. J Mater Res 17 (7), 1651–1654.

Schuh, C.A., Hufnagel, T.C., Ramamurty, U., 2007a. Mechanical behavior of amorphous alloys. Acta Mater. 55 (12), 4067–4109.

Schuh, C.A., Hufnagel, T.C., Ramamurty, U., 2007b. Mechanical behavior of amorphous alloys. Acta Mater. 55, 4067–4109.

Sha, Z., Wong, W.H., Pei, Q., Branicio, P.S., Liu, Z., Wang, T., Guo, T., Gao, H., 2017. Atomistic origin of size effects in fatigue behavior of metallic glasses. J. Mech. Phys. Solids 104, 84–95.

Shan, Z., Li, J., Cheng, Y., Minor, A., Asif, S.S., Warren, O., Ma, E., 2008. Plastic flow and failure resistance of metallic glass: insight from in situ compression of nanopillars. Phys. Rev. B 77 (15), 155419.

Shi, Y., Falk, M.L., 2005. Strain localization and percolation of stable structure in amorphous solids. Phys. Rev. Lett. 95 (9), 095502.

Shimizu, F., Ogata, S., Li, J., 2007. Theory of shear banding in metallic glasses and molecular dynamics calculations. Mater. Trans. 48 (11), 2923–2927.

Spaepen, F., 1977. A microscopic mechanism for steady state inhomogeneous flow in metallic glasses. Acta Metall. 25 (4), 407–415.

Sun, B., Pauly, S., Tan, J., Stoica, M., Wang, W., Kühn, U., Eckert, J., 2012. Serrated flow and stick–slip deformation dynamics in the presence of shear-band interactions for a Zr-based metallic glass. Acta Mater. 60 (10), 4160–4171.

Tao, W., Cao, P., Park, H.S., 2018. Atomistic simulation of the rate-dependent ductile-to-brittle failure transition in bicrystalline metal nanowires. Nano Lett. 18 (2), 1296–1304.

Wright, W.J., Liu, Y., Gu, X., Van Ness, K.D., Robare, S.L., Liu, X., Antonaglia, J., LeBlanc, M., Uhl, J.T., Hufnagel, T.C., et al., 2016. Experimental evidence for both progressive and simultaneous shear during quasistatic compression of a bulk metallic glass. J. Appl. Phys. 119 (8), 084908.

Wright, W.J., Schwarz, R.B., Nix, W.D., 2001. Localized heating during serrated plastic flow in bulk metallic glasses. Mater. Sci. Eng. 319, 229–232.

Yan, X., Gouissem, A., Guduru, P.R., Sharma, P., 2017. Elucidating the atomistic mechanisms underpinning plasticity in Li-Si nanostructures. Phys. Rev. Mater. 1 (5), 055401.

Yan, X., Sharma, P., 2016. Time-scaling in atomistics and the rate-dependent mechanical behavior of nanostructures. Nano Lett. 16 (6), 3487–3492.

Zhou, X., Zhou, H., Li, X., Chen, C., 2015. Size effects on tensile and compressive strengths in metallic glass nanowires. J. Mech. Phys. Solids 84, 130–144.

Zhu, T., Li, J., Samanta, A., Leach, A., Gall, K., 2008. Temperature and strain-rate dependence of surface dislocation nucleation. Phys. Rev. Lett. 100 (2), 025502.